JOURNAL OF GEOPHYSICAL RESEARCH, VOL. 116, A12217, doi:10.1029/2011JA016896, 2011

Convective and diffusive ULF wave driven radiation belt electron transport

A. W. Degeling,[1] R. Rankin,[1] and S. R. Elkington[2]

Received 1 June 2011; revised 9 September 2011; accepted 6 October 2011; published 15 December 2011.

[1] The process of magnetospheric radiation belt electron transport driven by ULF waves is studied using a 2-D ideal MHD model for ULF waves in the equatorial plane including day/night asymmetry and a magnetopause boundary, and a test kinetic model for equatorially mirroring electrons. We find that ULF wave disturbances originating along the magnetopause flanks in the afternoon sector can act to periodically inject phase space density from these regions into the magnetosphere. Closely spaced drift-resonant surfaces for electrons with a given magnetic moment in the presence of the ULF waves create a layer of stochastic dynamics for L-shells above 6.5–7 in the cases examined, extending to the magnetopause. The phase decorrelation time scale for the stochastic region is estimated by the relaxation time for the diffusion coefficient to reach a steady value. This is found to be of the order of 10–15 wave periods, which is commensurate with the typical duration of observed ULF wave packets in the magnetosphere. For L-shells earthward of the stochastic layer, transport is limited to isolated drift-resonant islands in the case of narrowband ULF waves. We examine the effect of increasing the bandwidth of the ULF wave driver by summing together wave components produced by a set of independent runs of the ULF wave model. The wave source spectrum is given a flat-top amplitude of variable width (adjusted for constant power) and random phase. We find that increasing bandwidth can significantly enhance convective transport earthward of the stochastic layer and extend the stochastic layer to lower L-shells.

Citation: Degeling, A. W., R. Rankin, and S. R. Elkington (2011), Convective and diffusive ULF wave driven radiation belt electron transport, *J. Geophys. Res.*, *116*, A12217, doi:10.1029/2011JA016896.

1. Introduction

[2] We examine the process of radiation belt electron energization driven by ULF waves. It is understood that energization in this case arises through the transport of electrons into regions of higher magnetic field strength, via drift-resonant interactions with the ULF waves [*Elkington et al.*, 1999], which preserves the first two adiabatic invariants and breaks the third invariant. Generally this has been considered a diffusive process, driven by a typically broad spectrum of ULF wave activity. However, it is often the case that ULF waves during CME and CIR driven storms have a strong monochromatic component. Moreover, the fast time scales of electron enhancements, as well as the appearance of phase space density (PSD) peaks and drift echoes phase-synchronized with ULF waves, indicate that occasionally electron transport may be convective rather than diffusive. This is important because observed departures from the diffusion paradigm are often cited as evidence of non-adiabatic energization processes [*Green and Kivelson*, 2004; *Chen et al.*, 2007]. The purpose of this article is to examine the effect of narrowband ULF waves on radiation belt electron dynamics, taking into account magnetospheric day/night asymmetry, and geometry of the magnetopause on (1) ULF wave propagation and source location, and (2) guiding center drift paths of equatorially mirroring electrons in the presence of these waves. This extends previous work of *Degeling et al.* [2007], *Degeling and Rankin* [2008], and *Degeling et al.* [2008], which considered symmetric magnetic field models in dealing with electron transport. In these previous studies, it was shown that interactions with ULF waves can give rise to convective electron transport across a wide range of L-shells that remains coherent over time scales of multiple wave periods, and can lead to the growth of peaks in electron PSD. We investigate whether this behavior persists when a more realistic magnetic geometry and ULF wave structure are considered for the case of narrowband ULF waves. We also consider the effect of increasing the ULF wave bandwidth on the electron dynamics.

[3] Section 2 of this paper describes first the ULF wave model, which uses a finite element model algorithm to solve the ideal MHD wave equations in the equatorial plane. An example scenario for ULF wave excitation is described in section 3, in which a distributed source of coherent ULF wave power across the dayside magnetopause is shown to

---

[1] Department of Physics, University of Alberta, Edmonton, Alberta, Canada.

[2] Laboratory for Atmospheric and Space Physics, University of Colorado, Boulder, Colorado, USA.

0148-0227/11/2011JA016896

give rise to a broad spectrum of azimuthal modes (*m*) within the magnetosphere. Low *m* MHD fast modes form a standing wave structure across the dayside magnetosphere and couple to a toroidal mode field line resonance (FLR) in the morning and afternoon sectors, while shorter wavelength (higher *m*) MHD fast modes propagate along the dawn and dusk flanks close to the magnetopause. The electron transport model is outlined in section 4, before describing the effect of the ULF waves on electron dynamics in section 5. Both the asymmetric magnetic field and the broad m-spectrum of ULF waves have a significant impact on the electron dynamics, giving rise to multiple overlapping drift-resonance islands which lead to stochasticity, particularly at high L-shells. As L-shell is decreased the separation between resonances increases, which can lead to the stable trapping of electrons within isolated resonance island chains. Within stochastic regions, it is expected that the electron dynamics can be described statistically by as a diffusive process on time scales much longer than the phase de-correlation time scale. This time scale is estimated by the time for the radial diffusion coefficient D_{LL}, which is calculated as a function of L-shell and time, to become time-stationary under the constant driving by ULF waves. Last, we introduce a closely spaced spectrum of ULF wave frequencies with a flat amplitude profile, and examine how changes in the bandwidth of this spectrum affect the electron dynamics.

2. The ULF Wave Model

[4] Starting from the plasma ideal MHD equations, the following linear equations can be obtained for low frequency waves:

$$\frac{\partial \mathbf{b}}{\partial t} = -\nabla \times \mathbf{E} \tag{1}$$

$$\frac{1}{v_A^2}\frac{\partial \mathbf{E}}{\partial t} = (\nabla \times \mathbf{b})_\perp - \frac{(\mu_o \mathbf{J} \times \mathbf{b}) \times \mathbf{B}}{B^2} + \mu_o \mathbf{J}^{ext} \tag{2}$$

where **b** and **E** are perturbed magnetic and electric fields, respectively, $\mu_o \mathbf{J} = \nabla \times \mathbf{B}$ is the background current density, v_A is the Alfvén speed and $\mathbf{J}^{ext}$ is a perpendicular current source term for launching waves. As shown by *Allan and Knox* [1979] for dipole fields and by *Degeling et al.* [2010] for compressed dipole fields, these equations can be arranged such that terms describing field aligned (shear Alfvén wave) eigenfunctions appear on the left-hand side, while terms describing the coupling of power across field lines through the MHD fast wave appear on the right-hand side.

[5] In previous work [*Degeling et al.*, 2010], a spectral method was used to describe the ULF wave solutions in terms of shear Alfvén waves (SAWs) along field lines, and decompose the equatorial amplitudes of these coupled waves in terms of a set of azimuthal modes. This method, however, was limited to a restricted range in azimuthal mode number *m*. Moreover, the outer boundary in the model was necessarily a closed oval shaped curve in the equatorial plane, which resembled the magnetopause only close to local noon. In this paper our primary interest in modeling the ULF waves is the inclusion of the magnetopause geometry, such that wave solutions are bound on the dayside and dawn/dusk flanks by a parabolic magnetopause, and are unbounded on the night side. We therefore make no assumptions about azimuthal mode structure and solve the "2-D plus t" partial differential equations for the equatorial amplitudes. We make the expedient approximation of a "box model" magnetic field geometry [*Zhu and Kivelson*, 1988], in order to simplify the treatment of SAW eigenfunctions along magnetic field lines. That is, for the purposes of this paper we assume that magnetic field lines are everywhere straight, and are terminated in flat conducting surfaces (representing the north and south ionospheres) a fixed distance ($z_{fl}/2$) above and below the equatorial plane. This assumption retains the basic physics of linear mode coupling between MHD fast waves and SAWs to form field line resonances (FLRs); however, the equatorial polarization properties of the FLRs [*Kabin et al.*, 2007] are simplified. The extension of this model to realistic closed magnetic field geometries is an area of continuing research.

[6] In this case, using Cartesian coordinates (x, y, z) (with z parallel to the magnetic field and normal to the equator, such that $\mathbf{B_o} = B_o(x{,}y)^{\mathbf{z}}$), the above wave equations can be written in component form as follows:

$$\left(\frac{\partial^2}{\partial z^2} - \frac{1}{v_A^2}\frac{\partial^2}{\partial t^2}\right)\begin{pmatrix} E_x \\ E_y \end{pmatrix} = \frac{1}{B_o}\begin{pmatrix} -\partial/\partial y \\ \partial/\partial x \end{pmatrix}\left(B_o\left(\frac{\partial E_x}{\partial y} - \frac{\partial E_y}{\partial x}\right)\right) + \mu_o \frac{\partial}{\partial t}\begin{pmatrix} J_x^{ext} \\ J_y^{ext} \end{pmatrix} \tag{3}$$

Under the box model assumption, all field aligned eigenfunctions are decoupled and any distinction between toroidal and poloidal shear wave polarizations and eigenfrequencies are lost. This enables linearly independent solutions satisfying conducting ionospheric boundary conditions to be described simply by $\mathbf{E} = \mathbf{E}_n(x, y)\, cos(k_n z)\, exp(-i\omega t)$, where $k_n = n\pi/z_{fl}$, (n = 1, 2..), which reduces equation (3) to a pair of coupled elliptic partial differential equations for E_{nx} and E_{ny}.

[7] These equations are solved using a two dimensional finite element method (FEM) solver in the Matlab Partial Differential Equation (PDE) Toolbox (see http://www.mathworks.com/help/pdf_doc/pde/pde.pdf). This software uses a basis of tent functions defined on an unstructured triangular mesh to approximate the solution to the weak form of the PDE using the Galerkin method [*Braess*, 2001].

[8] Figure 1a shows the computational domain and density of triangles used in the model. The triangular mesh is automatically refined by the numerical solver, resulting in a high triangle density along field line resonance surfaces. The solid black line in Figure 1 marks the magnetopause location on the dayside and morning/evening flanks, and an artificial boundary on the night-side, and defines the region of interest in this model. Outside this boundary, wave solutions are artificially damped in order to minimize reflections from the numerical outer boundary. This allows the magnitude of the electric field at the outer boundary to be set to zero. The inner boundary, which is set at a radius of 2 R_E, is located well within the MHD fast wave turning point, allowing the electric field magnitude to be set to zero here also. The damping of waves in the model arises through the inclusion of an imaginary part to the driver frequency $\omega = \omega_R - i\omega_I$. Strong damping outside the region of interest within the

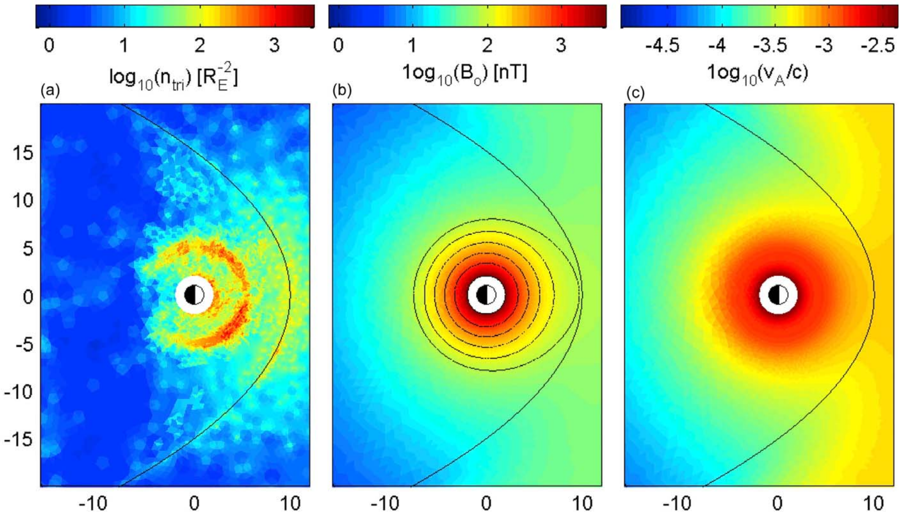

Figure 1. The ULF wave model domain and input parameters in the equatorial plane: (a) triangle mesh density; (b) magnetic field strength; and (c) Alfvén speed. The parabolic solid black line marks the magnetopause, and the elliptical solid lines in Figure 1b mark contours of constant L_o^*.

magnetosphere is produced by setting $\omega_I/\omega_R \gg 1$, while weak damping within this region to mimic finite ionospheric Pederson conductivity is given by setting $\omega_I/\omega_R = 0.1$.

[9] A simplified version of the vacuum magnetic field model of *Stern* [1985] is used to provide the equatorial magnetic field inside the magnetosphere. This model considers the magnetopause as a conducting paraboloid shell, and solves Laplace's equation in parabolic coordinates for the magnetic potential γ associated with a curl-free magnetic field ($\mathbf{B} = -\nabla\gamma$), using the boundary condition that the Earth's dipole field is perfectly shielded by surface magnetopause currents (see *Degeling et al.* [2010] for more details on our implementation of the model). We use the same approach to match a constant interplanetary magnetic field (IMF) directed along z to the magnetopause. If the magnetic potentials interior and exterior to the magnetosphere are respectively γ_E and γ_{IMF} then the magnetic field in the equatorial plane ($z = 0$) in our model is given by

$$B = \sigma\nabla\gamma_E + (1-\sigma)\nabla\gamma_{IMF} \tag{4}$$

where $\sigma = \sigma(x, y)$ is a step function smoothed over a finite width (set to 0.25 R_E) perpendicular to the magnetopause, such that $\sigma = 1$ inside the magnetosphere and smoothly decreases to zero outside. The model magnetic field is shown in Figure 1b. The location and shape of the parabolic magnetopause boundary are specified by radial stand-off distances from the center of the Earth along the dawn/dusk and noon meridians. These are set to 15 R_E and 10 R_E, respectively in all cases in this article.

[10] The equatorial plasma density is specified using the same parametric model that was used by *Degeling et al.* [2010]. This model assumes power law scalings with L-shell for the plasma density inside and outside the plasmapause, and smoothly joins the two solutions across a specified width in L-shell representing the plasmapause. For example, the inner and outer edges of the plasmapause are located at $L = 3$ and $L = 6$ in all cases shown, at which plasma density values of ρ = 2000 and ρ = 150 amu/cm^3 are set, with scaling indicies $n = -2$ and $n = -1$, respectively.

[11] The equatorial Alfvén speed $v_A = B/\sqrt{\rho}$ derived from the magnetic field and plasma density profile detailed above is shown in Figure 1c, which shows that the plasmapause is relatively weak in this example, in that the density gradient with L-shell is insufficient to cause a localized peak in v_A across the plasmapause location (as would be expected for a strong density drop at the plasmapause [*Allan and Poulter*, 1992]). Therefore, the Alfvén continuum of eigenfrequencies monotonically decreases as a function of L-shell, such that a constant frequency driver is expected to give rise to a single field line resonance for a given eigenmode. Note that the form of the solution to equation (3) along the magnetic field corresponds to a set of even functions for the electric field, giving anti-nodes in the equatorial plane for E_x and E_y, and therefore b_z, whereas b_x and b_y have nodes in the equatorial plane.

3. The ULF Wave Excitation From the Dayside Magnetopause

[12] For the purposes of this study, an external oscillating current J^{ext} with a specified frequency of 3 mHz is placed along the magnetopause boundary in the model, directed tangential to the boundary and perpendicular to the magnetic field. The current amplitude is specified by a Gaussian profile in directions along and across the magntopause, with full-width-half-maxima of 5 R_E and 1 R_E, respectively. This current excites a displacement in the direction perpendicular to the magnetopause, launching an MHD fast wave into the magnetosphere (a sunward propagating wave is also launched outside the magnetopause; however, this wave is strongly damped as described in section 2). As such, this excitation mechanism mimics oscillations in the day-side magnetopause location that might be expected from buffeting due to variations in solar wind dynamic pressure.

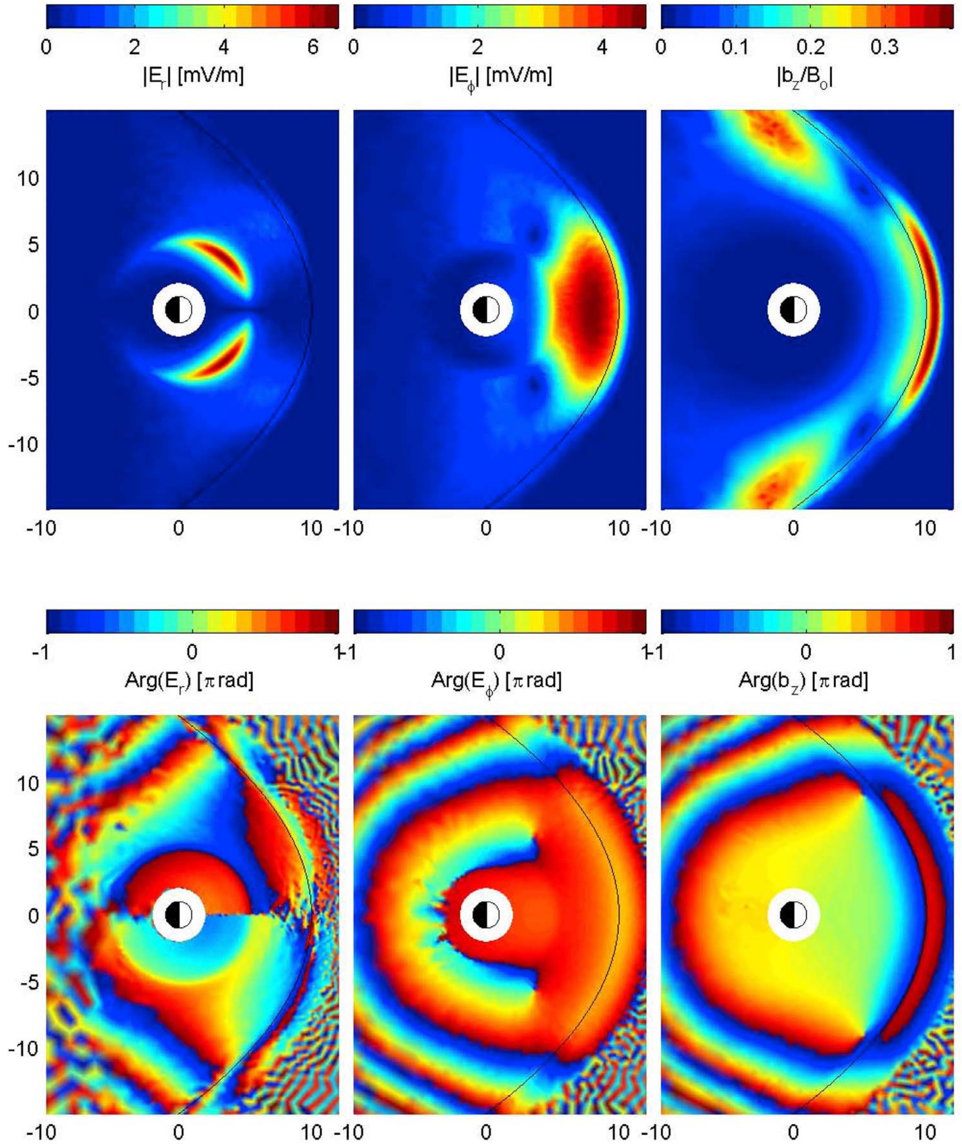

Figure 2. The (top) amplitude and (bottom) phase of ULF wave model outputs for a 3 mHz ULF wave source along the dayside magnetopause peaked at local noon, showing (left) E_r (mV/m), (middle) E_ϕ (mV/m), and (right) the ratio b_z/B_o.

[13] Figure 2 shows the amplitude and phase of the azimuthal and radial electric fields, as well as the ratio of the wave magnetic field to the background field. Figure 2 shows the expected behavior for the coupling of a low azimuthal mode number MHD fast mode to an FLR in the inner magnetosphere, and also the tailward propagation of MHD fast modes along the dawn and dusk flanks. The FLR is evidenced by a strong peak in the radial electric field amplitude, accompanied by a phase change of close to π radians across the peak. The width of the resonance and extent of the phase change are dependent on the ratio ω_I/ω_R. As this ratio is decreased (not shown), the resonance peak becomes sharper and the phase change across the peak more closely approaches π radians.

[14] An interesting feature in Figure 2 is the appearance of large amplitude fast mode waves close to the magnetopause boundary. These waves bear a resemblance to features one might expect from Kelvin-Helmholtz (K-H) instability driven waveguide modes [*Walker*, 1981; *Allan and Wright*, 1997]; however, there is no physics related to shear-flows included in this model. Rather, these waves are the result of the focusing of wave power along the semi-reflective flanks of the magnetopause. As this is a linear model, the amplitude of waves within the magnetosphere is strictly controlled by the source amplitude. The case shown, in which the peak electric field is about 6 mV/m at the FLR and $b_z/B_o \approx 0.4$ along the magnetopause flanks, represents the maximum wave amplitude considered in this article. For comparison, PC5 FLRs with equatorial electric field amplitudes of the order of 1–3 mV/m are typical, however in situ observations of ULF waves with amplitudes up to and greater than 5 mV/m near the equatorial plane have also been reported [e.g., *Ozeke*

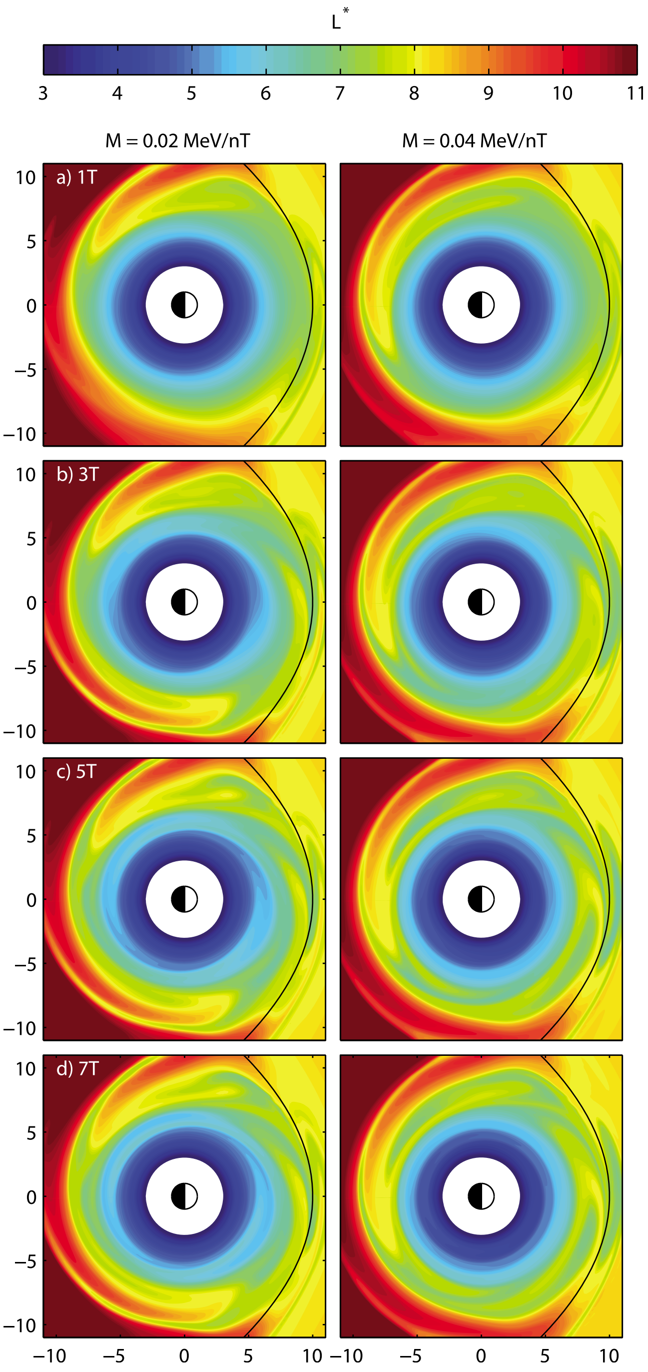

Figure 3. (a–d) Still frames of the electron transport model output, showing the mapping of $L_o^*(r, \phi, M, t)$ in response to the 3 mHz wave shown in Figure 2 as a function of time, for (left) $M = 0.02$ MeV/nT and (right) $M = 0.04$ MeV/nT. The time in wave periods (T) is shown in each plot.

et al., 2009; *Glassmeier and Junginger*, 1987; *Junginger et al.*, 1984; *Sarris et al.*, 2009; *Zong et al.*, 2009; *Tan et al.*, 2011].

4. Equatorially Mirroring Electron Dynamics

[15] We consider the simplified dynamics of equatorially mirroring electrons. The guiding center equation of motion [*Northrop*, 1963] is applicable for these electrons under the influence of ULF waves, whose frequencies are much lower than the electron gyrofrequency, and is given by

$$\mathbf{v} = \frac{\mathbf{E}\times\mathbf{B}}{B^2} + \frac{M}{q\gamma}\frac{\mathbf{B}\times\nabla B}{B^2} \tag{5}$$

where the magnetic moment M is a constant of motion, q is the electronic charge and $\gamma = (1 + 2MB/m_e c^2)^{1/2}$ is the relativistic correction factor.

[16] We use this equation to drive a test-kinetic simulation for markers of constant electron PSD $f = f(r, \phi, M, J, t)$, (where the second adiabatic invariant J is set equal to zero for equatorially mirroring electrons). We assume that an initial unperturbed distribution of the form $f = f(L_o^*, M)$ exists, where $L_o^* = (B(r,\phi)/B_{eq})^{(-1/3)}$ is the initial L-shell parameter representing the third invariant for equatorially mirroring electrons (where B_{eq} is the Earth's magnetic field strength at the equator), which is assumed to be conserved prior to the onset of ULF wave activity. In principle we could calculate f by solving the advection equation for PSD given by Liouville's theorem [*Northrop*, 1963]. However, since we are interested in transport characteristics, such as diffusion in L-shell, we instead consider the initial L-shell L_o^* as a marker for contours of constant PSD, and calculate the two-dimensional mapping of L_o^* to later times. That is, we solve the advection equation for $L_o^* = L_o^*(r,\phi,t)$:

$$\frac{\partial L_o^*}{\partial t} + \mathbf{v}\cdot\nabla L_o^* = 0 \tag{6}$$

where M is held constant in the calculation of $\mathbf{v}$ by equation (5). This is done numerically on a fixed polar coordinate grid using an operator splitting algorithm (for the r and ϕ directions) in conjunction with a 1-D flux corrected transport algorithm [*Jardin*, 2010]. In this procedure, the ULF wave data is interpolated once from the unstructured triangular grid to the polar coordinate grid. Once the mapping of L_o^* is known, the corresponding value of f may be calculated from the assumed initial distribution, for electrons with initial positions within the magnetosphere. Solving for L_o^* instead of f has the advantage that it enables an expedient calculation of the diffusion coefficient D_{LL} as a function of time:

$$D_{LL}(L^*, t) = \frac{1}{2\pi(t - t_o)} \oint_{L^*} \left(L^*(B_o(r,\phi)) - L_o^*(r,\phi,t)\right)^2 d\phi \tag{7}$$

The first term inside the brackets of the integrand is the L^* value for each (r,ϕ) grid point, the second term is the initial value of L^* that advected to the same coordinates (r,ϕ) after time t, hence the integrand is $(\Delta L^*)^2$. Note that the integration over ϕ is carried out along an L^* = const contour.

5. Results

5.1. ULF Wave Driven Electron Transport

[17] Figure 3 shows the time-dependent mapping of L_o^* under the action of ULF waves shown in Figure 2, with the magnetic moment M set to 0.02 and 0.04 MeV/nT, respectively, in the left and right columns. A series of still-frames are shown in each column in Figure 3, advancing time by two wave periods each frame. The first frame, corresponding

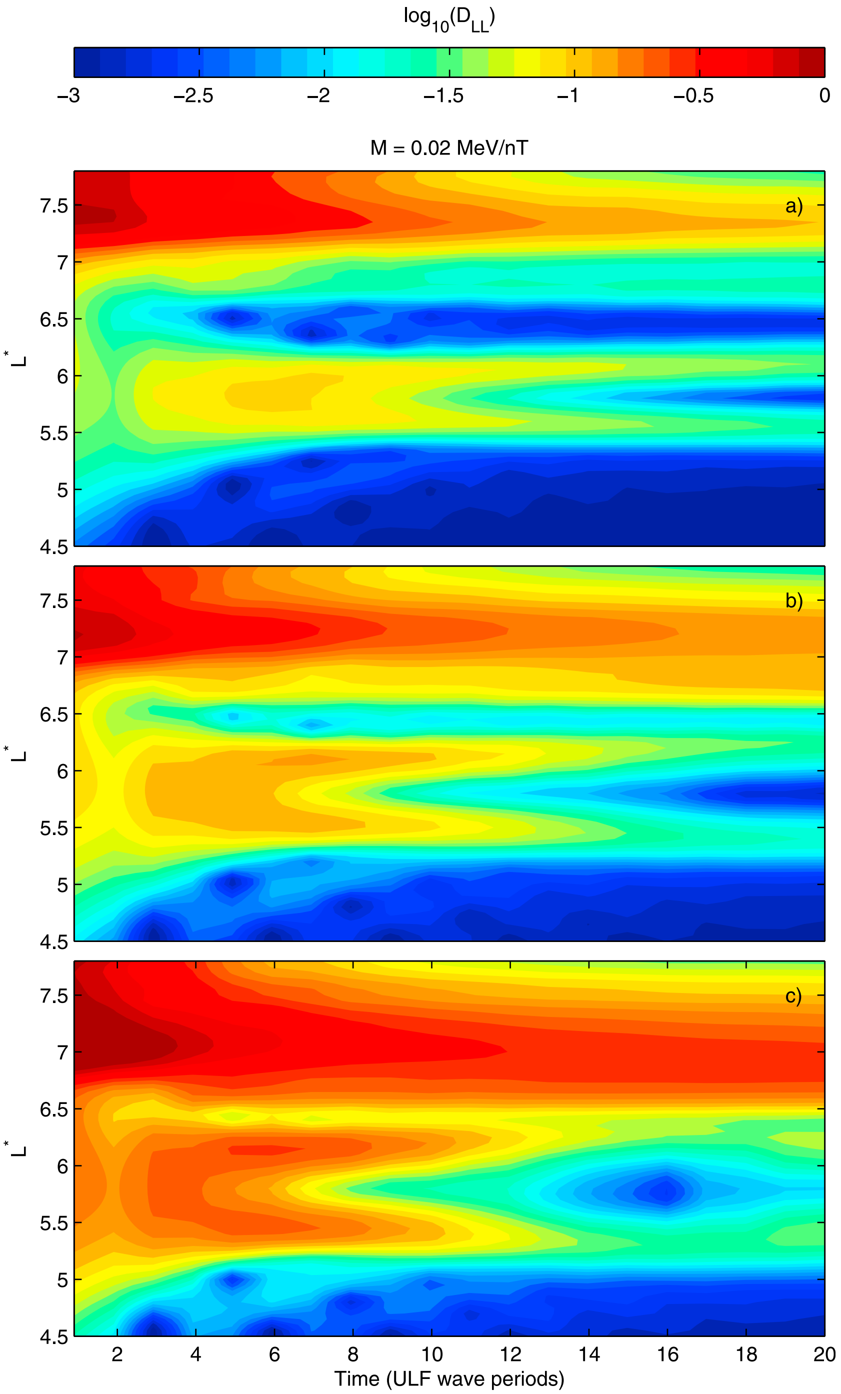

Figure 4. Calculation of the diffusion coefficient D_{LL} given in equation (7), shown as a function of time and L^*, for three ULF wave amplitude settings, corresponding to 1/3×, 2/3×, and 1× the wave value used to produce Figure 2.

to one wave period after the onset of ULF waves, shows an initial injection in the afternoon sector of markers originating at L-shells corresponding to the magnetopause. Subsequent frames show the shearing of these pulses as they drift across the night-side, before being re-enforced by further injections upon their return to the afternoon sector, such that the left-hand case appears to show an $m = 3$ resonance structure, while the right-hand case shows an $m = 2$ resonance structure. These resonance structures appear to become increasingly folded and complex with time, and close inspection shows that this is due to mixing with a neighboring $m = 4$ ($m = 3$) resonance in the left (right) case, similar to that given by *Degeling et al.* [2007]. Another low m resonance is visible at lower L-shell in each column; however, these are clearly separate from the overlapping resonances at higher L-shell.

[18] It is well known that overlapping resonances give rise to stochastic dynamics, and may be modeled as a diffusive process on time scales much longer than the phase

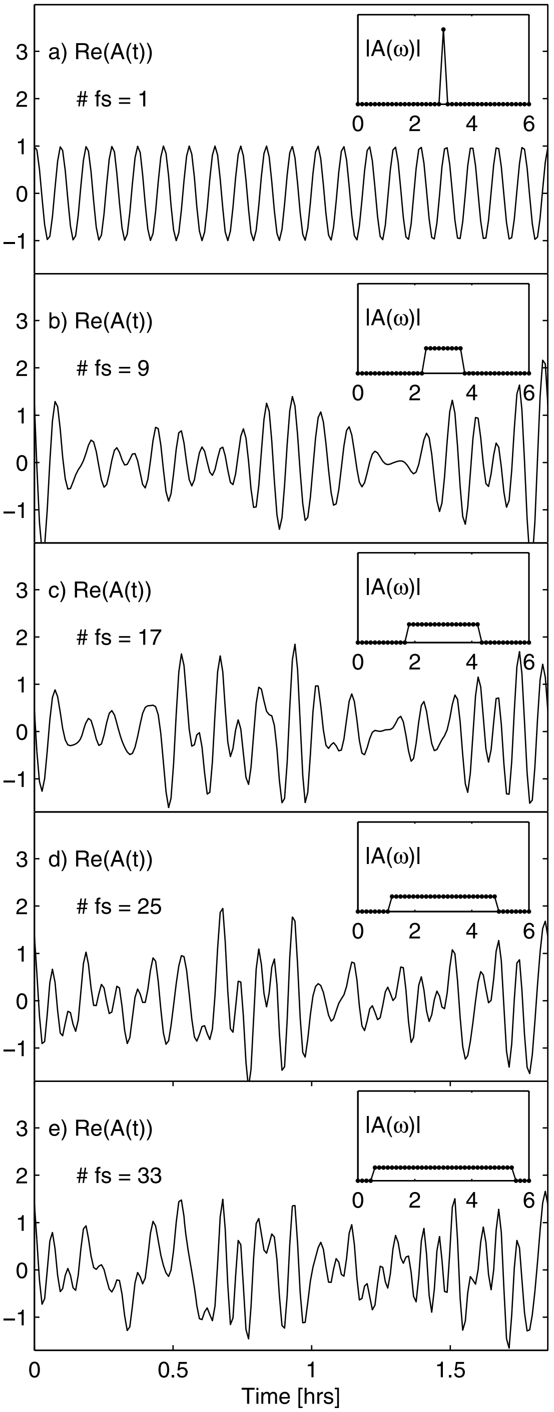

Figure 5. The input perturbations used to drive the ULF wave model, scanning the five spectral bandwidth from cases. The inset in each plot shows the amplitude spectrum $|A_n(\omega_n)|$ used to weight each frequency component (ω_n), and each plot itself shows the real part of the resulting time domain signal. The number of frequency components with nonzero amplitude (“# fs”) are indicated. For all cases the total signal power is kept constant, such that $\sum (A_i(\omega_i))^2 = 1$.

de-correlation time scale [*Lichtenberg and Lieberman*, 1992]. This time scale may be estimated by the time taken for the diffusion coefficient given by equation (7) to reach a constant value, when under the action of a constant amplitude driver. Figure 4 shows examples of this calculation for the $M = 0.02$ MeV/nT case shown in Figure 3, with the ULF wave source amplitude increasing from Figure 4a to 4c. The y-axis in Figures 3 and 4 is L^*, the x-axis is time, and the colors represent values of $\log_{10}(D_{LL})$. In Figure 4a, D_{LL} for a range of L^* values above 6.6 is shown to decrease toward a stationary value. At lower L^*, two strong peaks in D_{LL} with L^* appear within the first 5 wave periods, which subsequently decay in time. As the ULF wave amplitude is increased in Figures 4b and 4c, the D_{LL} profile for $L^* > 6.5$ is shown to relax to a constant non-zero value over 15 and 12 wave period time scales, respectively. The lower L-shell profile for D_{LL} also evolves on a faster time scale; however, it does not approach a steady state, and appears to show a long time scale modulation in Figure 4c.

[19] The behavior at high L-shell is the expected behavior for a stochastic dynamical system (resulting from the overlapping resonances apparent in Figure 3), in which phase correlations in the dynamics are lost with time. The lower L-shell behavior indicates the transport across a limited band in L-shell arising from the isolated $m = 2$ resonance island. As the amplitude is increased in Figures 4b and 4c, the threshold L^* value for stochastic behavior decreases, as does the time scale for the dynamics to become diffusive within this region. The width in L-shell of the $m = 2$ resonance is also shown to increase, and the trapping period for the resonant electrons becomes apparent, giving rise to the modulation in D_{LL}. If the amplitude of the ULF wave were to be further increased it could be expected that resonance overlap would occur between the $m = 2$ resonance and higher m resonances at higher L-shell.

[20] Figure 4 demonstrates that, at least in the case of a narrowband ULF wave source, the stochasticity arising from introduction of multiple resonances through both the localization of the ULF wave source [*Degeling et al.*, 2007] and the inclusion of day/night asymmetry in electron drift motion [*Elkington et al.*, 2003] loses phase correlation gradually over multiple wave periods, on a time scale of the order of a typical ULF wave packet. Therefore, the adoption of a diffusive description, where the loss of phase correlation is assumed a priori, would be inappropriate in this case.

5.2. Increasing ULF Wave Source Bandwidth

[21] We now turn to scenarios where the ULF wave source has non-zero bandwidth. This is done by using the ULF wave model to calculate electromagnetic fields in response to a set of ULF wave drivers, each with identical source geometries arranged along the magnetopause (the same source geometry that produced Figure 2), with each source driven at a different discrete frequency between 0.15 and 6.0 mHz, with a spacing of 0.15 mHz. A flat-top spectrum of amplitudes and randomly assigned phases are assigned to the sources, and the resulting wavefields are interpolated onto the polar-coordinate grid and summed to give the inputs to the test-kinetic electron transport model. Figure 5 shows the input ULF source spectrum of amplitudes and resulting ULF wave time series for a set of cases where the spectral bandwidth is increased, keeping the total power (the sum of the amplitudes squared) constant. The same randomly generated phase spectrum is used in each of these cases, in order to allow comparisons to be made from case to case. As can be expected, Figure 5 shows that the introduction of spectral

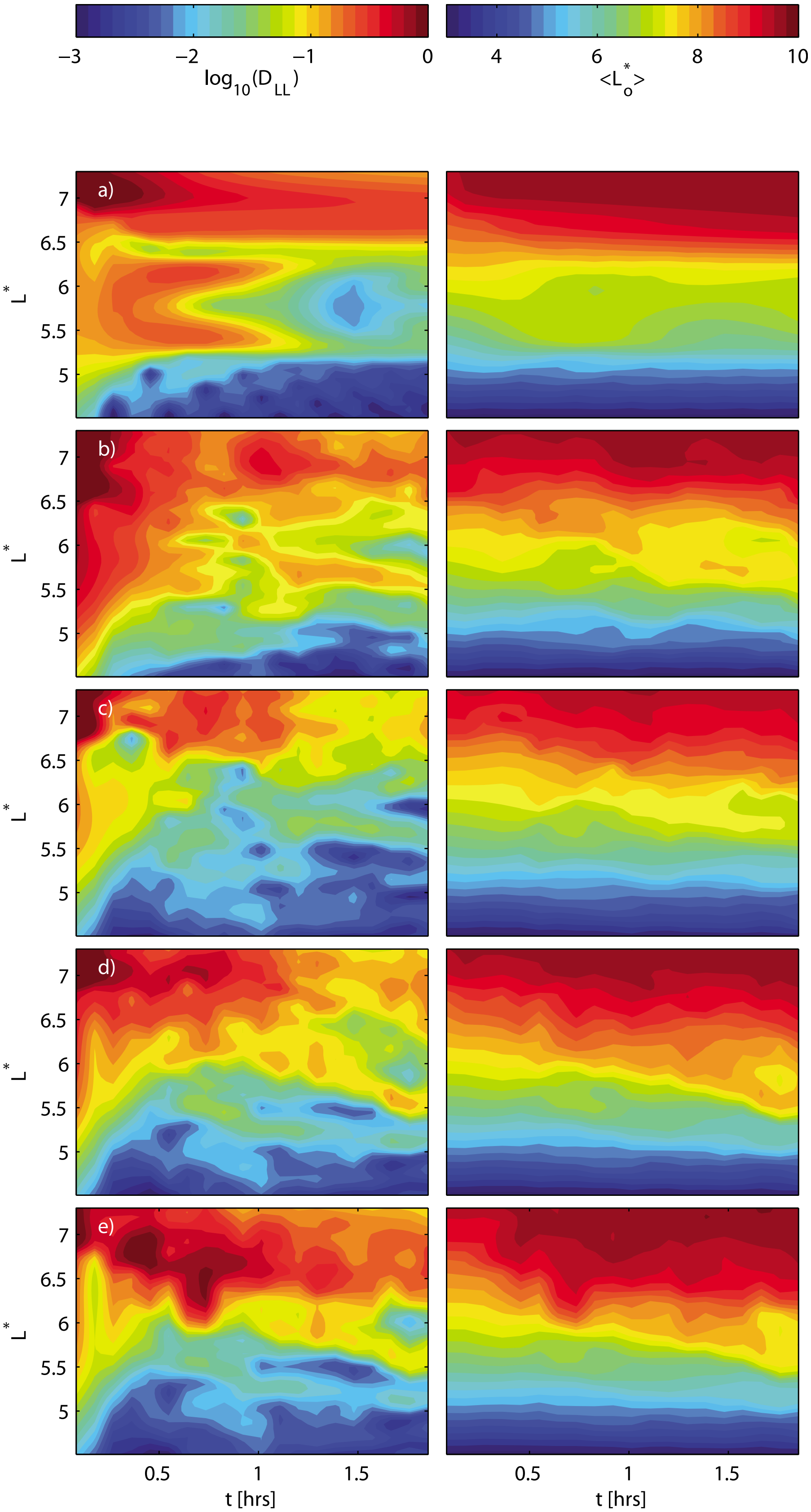

Figure 6. Calculation of (left) D_{LL} and (right) $\langle L_o^* \rangle$ for electrons with $M = 0.02$ MeV/nT, for the five cases with increasing spectral bandwidth shown in Figure 5.

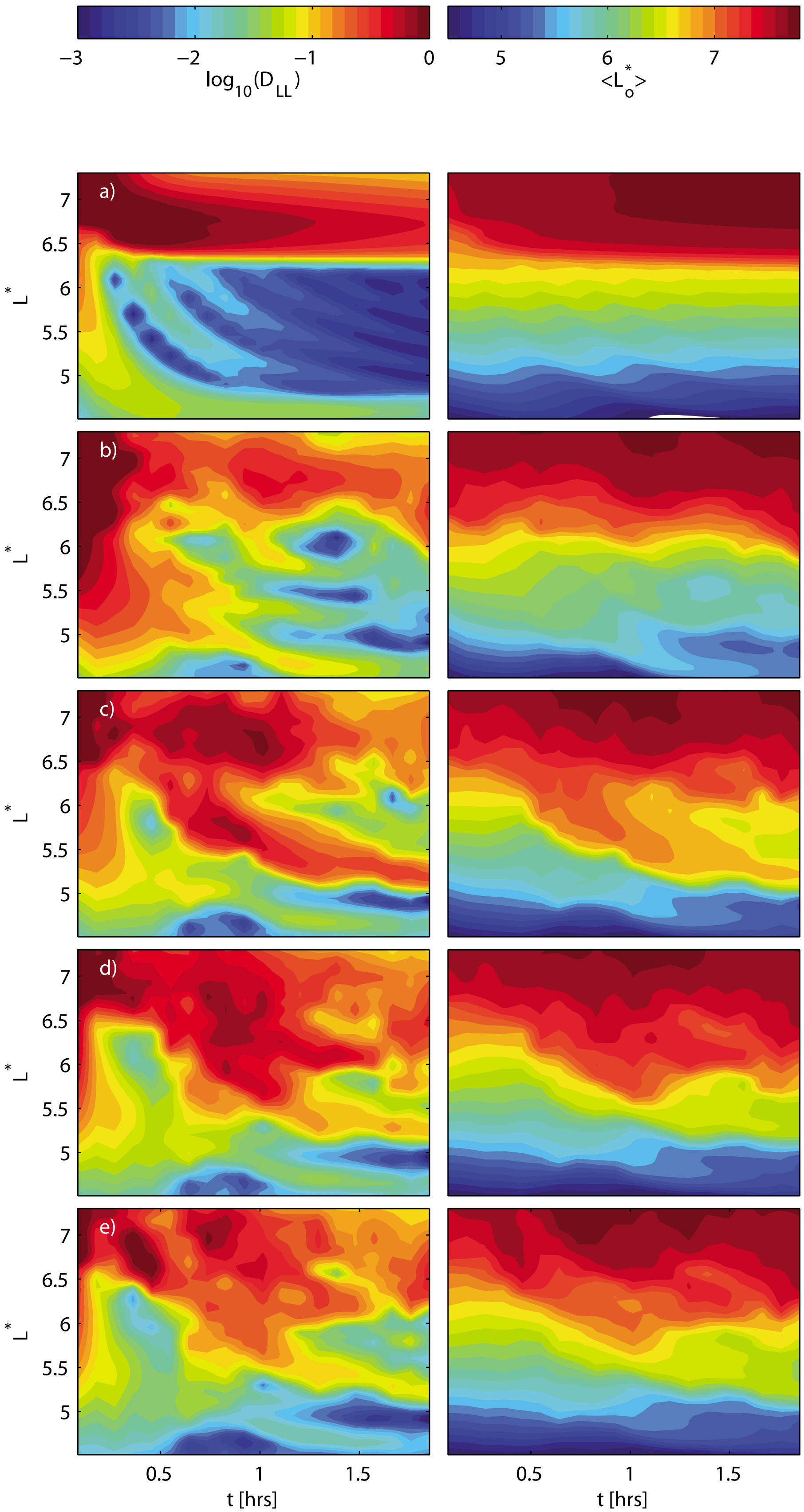

Figure 7. Calculation of (left) D_{LL} and (right) $\langle L_o^* \rangle$ for electrons with $M = 0.04$ MeV/nT, for the five cases with increasing spectral bandwidth shown in Figure 5.

bandwidth gives rise to wave packets in the time series that become increasingly bursty and unstructured as the bandwidth is increased. Figures 6 and 7 show results from the transport model for magnetic moments 0.02 and 0.04 MeV/nT, respectively. The five rows in Figures 6 and 7 correspond with cases shown in Figures 5a–5e. The left-hand columns in Figures 6 and 7 show D_{LL} calculated as a function of time (as in Figure 4). As the bandwidth is increased these plots show an increase in fluctuations in D_{LL} with time across most L-shells, which makes an interpretation on whether the dynamics are diffusive based on the stationarity of D_{LL} difficult. For this reason, the value $\langle L_o^* \rangle$, which is L_o^* averaged along an $L^* = const$ contour over ϕ is plotted as a function of time and L^* in the right-hand columns of Figures 6 and 7.

[22] The parameter $\langle L_o^* \rangle$ is introduced because it allows us to distinguish between diffusive and non-diffusive dynamics. For example, $\langle L_o^* \rangle$ is formally equivalent to $\langle f(M, L_o^*) \rangle$ in the special case where $f(M, L_o^*)$ is a linear function of L_o^*, in which case, a variation of $\langle L_o^* \rangle$ with time that exhibits a growing localized peak indicates non-diffusive behavior because it implies a similar growing peak in $\langle f(M, L_o^*) \rangle$ [*Degeling et al.*, 2008]. Hence the formation of a growing peak in $\langle L_o^* \rangle$ indicates non-diffusive dynamics. In general, the direction of net transport of PSD (leading to an enhancement or dropout in average PSD with time at a given L^*, or the formation of localized peaks in PSD), is dependent upon the initial PSD profile $f(M, L_o^*)$, but this is a different question to whether or not the electron dynamics are diffusive.

[23] Examples of growing peaks in $\langle L_o^* \rangle$ are found in Figure 6b and Figure 7c. In each case, these peaks occur on L-shells lower than 6.5, where the behavior is clearly non-diffusive in the narrowband case (Figures 6a and 7a).

[24] One might ask how these peaks, which can be shown to result from the $m = 2$ and $m = 1$ drift-resonances for $M = 0.02$ and 0.04 MeV/nT (Figures 6 and 7), respectively, can occur in the presence of multiple frequency components, each with overlapping resonance islands. The answer appears to be given by examining the time series in Figure 5. The formation of the peak by $M = 0.02$ MeV/nT electrons in Figure 5b appears to be preceded by a well defined wave packet with a consistent 3 mHz frequency that persists for over half an hour. The strong peak formed by $M = 0.04$ MeV/nT electrons in Figure 5c follows a burst of four large amplitude oscillations over a half-hour interval. In both cases it appears that these particular wave packets are sufficiently narrowband to give rise to regular trapping behavior rather than stochastic behavior. That is, the trapping widths for each resonance corresponding to the frequency components that constructively interfere to give these wave packets is sufficiently large to include each of the other resonances, such that they form a single common trapping regime (for example, similar to *Lichtenberg and Lieberman* [1992, Figure 5.25(c)]). As the bandwidth is increased in both examples the peaks in $\langle L_o^* \rangle$ become degraded and smoothed out. This is because the trapping widths of each resonance decreases as bandwidth is increased (since each frequency component is lower in amplitude to keep the total power constant). Therefore, the partial overlap between these resonances causes a wide band of stochasticity that extends from high L-shell down to $L^* = 5.5$ for both $M = 0.02$ and 0.04 MeV/nT in Figure 5e) (similar to *Lichtenberg and Lieberman* [1992, Figure 5.25(b)]).

[25] The plots of D_{LL} for this case, shown in Figures 6e and 7e, show fluctuations during the first hour, which gradually decay to a more or less steady value in the second hour shown in the plot. This indicates that, even in this relatively broadband case, the time scale for phase de-correlation appears to be of the order of an hour. This result, plus the findings of non-diffusive characteristics discussed above, argue against the use of diffusion models for studying the response radiation belt electron to externally driven ULF waves, particularly in cases where wave packet structure are identifiable in the ULF data.

6. Conclusions

[26] In this article, we have studied the process of magnetospheric radiation belt electron transport driven by ULF waves, using an ideal MHD model for ULF waves in the equatorial plane coupled to a test kinetic model for equatorially mirroring electrons. Our results in this study, which includes the effect of day/night asymmetry and the geometry of the magnetopause on the excitation and propagation of ULF waves, and also the drift trajectories of equatorially mirroring electrons, are consistent with those of previous studies in a symmetric magnetic field. First, we find that a higher density of drift resonances occur as L-shell is increased, making it increasingly likely that island overlap will give rise to stochastic behavior at high L-shells. Second, we find that the time scale for phase de-correlation within the stochastic layer is of the order of 10 to 15 wave periods for the cases studied, which amounts to at least a significant fraction of the typical duration of a ULF wave packet in the magnetosphere. This limits the usefulness of characterizing radiation belt electron dynamics as a diffusive process in our view. Third, we introduce spectral bandwidth to the ULF wave source and find that it can give rise to an enhancement in convective transport, in some circumstances, and extends the stochastic layer to lower L-shell. The phase de-correlation time scale, however, appears to remain inconveniently large.

[27] **Acknowledgments.** The authors would like to thank John Shillington, Barton Satchwill, and Everett Toes of Cibera CESWP team for their enthusiastic computing infrastructure support, as well as Louis Ozeke, Jonathan Rae, and Clare Watt for constructive discussions. This work is partially funded by the Canadian Space Agency, Natural Sciences and Engineering Research Council of Canada, and the National Science Foundation.

[28] Robert Lysak thanks the reviewers for their assistance in evaluating this paper.

References

Allan, W., and F. Knox (1979), Dipole field model for axisymmetric Alfven waves with finite ionosphere conductivities, *Planet. Space Sci.*, *27*(1), 79–85.

Allan, W., and F. Poulter (1992), ULF waves—Their relationship to the structure of the Earth's magnetosphere, *Rep. Prog. Phys.*, *55*, 533–598.

Allan, W., and A. Wright (1997), Large-m waves generated by small-m field line resonances via the nonlinear Kelvin-Helmholtz instability, *J. Geophys. Res.*, *102*(A9), 19,927–19,933.

Braess, D. (2001), *Finite Elements*, 2nd ed., Cambridge Univ. Press, New York.

Chen, Y., G. D. Reeves, and R. H. W. Friedel (2007), The energization of relativistic electrons in the outer Van Allen radiation belt, *Nature*, *3*(9), 614–617, doi:10.1038/nphys655.

Degeling, A. W., and R. Rankin (2008), Resonant drift echoes in electron phase space density produced by dayside Pc5 waves following a geomagnetic storm, *J. Geophys. Res.*, *113*, A10220, doi:10.1029/2008JA013254.

Degeling, A. W., R. Rankin, K. Kabin, R. Marchand, and I. R. Mann (2007), The effect of ULF compressional modes and field line resonances on relativistic electron dynamics, *Planet. Space Sci.*, *55*(6), 731–742, doi:10.1016/j.pss.2006.04.039.

Degeling, A. W., L. G. Ozeke, R. Rankin, I. R. Mann, and K. Kabin (2008), Drift resonant generation of peaked relativistic electron distributions by Pc 5 ULF waves, *J. Geophys. Res.*, *113*, A02208, doi:10.1029/2007JA012411.

Degeling, A. W., R. Rankin, K. Kabin, I. J. Rae, and F. R. Fenrich (2010), Modeling ULF waves in a compressed dipole magnetic field, *J. Geophys. Res.*, *115*, A10212, doi:10.1029/2010JA015410.

Elkington, S., M. Hudson, and A. Chan (1999), Acceleration of relativistic electrons via drift-resonant interaction with toroidal-mode Pc5 ULF oscillations, *Geophys. Res. Lett.*, *26*(21), 3273–3276.

Elkington, S., M. Hudson, and A. Chan (2003), Resonant acceleration and diffusion of outer zone electrons in an asymmetric geomagnetic field, *J. Geophys. Res.*, *108*(A3), 1116, doi:10.1029/2001JA009202.

Glassmeier, K.-H., and H. Junginger (1987), Concerning the ionospheric modification of magnetospheric hydromagnetic waves: Case studies, *J. Geophys. Res.*, *92*(A11), 12,213–12,219.

Green, J. C., and M. G. Kivelson (2004), Relativistic electrons in the outer radiation belt: Differentiating between acceleration mechanisms, *J. Geophys. Res.*, *109*, A03213, doi:10.1029/2003JA010153.

Jardin, S. (2010), *Computational Methods in Plasma Physics*, CRC Press, New York.

Junginger, H., G. Geiger, G. Haerendel, F. Melzner, E. Amata, and B. Higel (1984), A statistical study of dayside magnetospheric electric field fluctuations with periods between 150 and 600 s, *J. Geophys. Res.*, *89*, 5495–5505.

Kabin, K., R. Rankin, I. R. Mann, A. W. Degeling, and R. Marchand (2007), Polarization properties of standing shear Alfven waves in non-axisymmetric background magnetic fields, *Ann. Geophys.*, *25*(3), 815–822.

Lichtenberg, A. J., and M. A. Lieberman (1992), *Regular and Chaotic Dynamics*, 2nd ed., Springer, New York.

Northrop, T. G. (1963), *The Adiabatic Motion of Charged Particles*, Interscience, New York.

Ozeke, L. G., I. R. Mann, and I. J. Rae (2009), Mapping guided Alfvén wave magnetic field amplitudes observed on the ground to equatorial electric field amplitudes in space, *J. Geophys. Res.*, *114*, A01214, doi:10.1029/2008JA013041.

Sarris, T. E., et al. (2009), Characterization of ULF pulsations by THEMIS, *Geophys. Res. Lett.*, *36*, L04104, doi:10.1029/2008GL036732.

Stern, D. P. (1985), Parabolic harmonics in magnetospheric modeling: The main dipole and the ring current, *J. Geophys Res.*, *90*(A11), 10,851–10,863.

Tan, L. C., X. Shao, A. S. Sharma, and S. F. Fung (2011), Relativistic electron acceleration by compressional mode ULF waves: Evidence from correlated Cluster, Los Alamos National Laboratory spacecraft, and ground-based magnetometer measurements, *J. Geophys. Res.*, *116*, A07226, doi:10.1029/2010JA016226.

Walker, A. D. M. (1981), The Kelvin-Helmholtz instability in the low-latitude boundary-layer, *Planet. Space Sci.*, *29*(10), 1119–1133.

Zhu, X., and M. G. Kivelson (1988), Analytic formulation and quantitative solutions of the coupled ULF wave problem, *J. Geophys. Res.*, *93*(A8), 8602–8612.

Zong, Q.-G., et al. (2009), Energetic electron response to ULF waves induced by interplanetary shocks in the outer radiation belt, *J. Geophys. Res.*, *114*, A10204, doi:10.1029/2009JA014393.

A. W. Degeling and R. Rankin, Department of Physics, University of Alberta, Edmonton, AB T6G 2G7, Canada. (degeling@phys.ualberta.ca)

S. R. Elkington, Laboratory for Atmospheric and Space Physics, University of Colorado, Boulder, CO 80303, USA.